$x_{B|A,\alpha} = x_B - \alpha x_A$, and $p_{B|E,\beta} = p_B - \beta p_E$. Because Alice's, Bob's and Eve's operators commute, we have $[x_{B|A,\alpha}, p_{B|E,\beta}] = [x_B, p_B]$, and thus the Heisenberg relation $\Delta x^2_{B|A,\alpha}\, \Delta p^2_{B|E,\beta} \geq N_0^2$. Defining the conditional variances as $V(x_B|x_A) = \min_\alpha\{\Delta x^2_{B|A,\alpha}\}$ and $V(p_B|p_E) = \min_\beta\{\Delta p^2_{B|E,\beta}\}$, we obtain $V(x_B|x_A)\, V(p_B|p_E) \geq N_0^2$, or, by exchanging x and p, $V(p_B|p_A)\, V(x_B|x_E) \geq N_0^2$.

Alice has the estimators (x_A, p_A) for the field $(x_{in}, p_{in}) = (x_A + A_x, p_A + A_p)$ that she sends, with $\langle A_x^2 \rangle = \langle A_p^2 \rangle = s N_0$. Here s measures the amount of squeezing possibly used by Alice in her state preparation[14], with $s \geq V^{-1}$ for consistency with Heisenberg's relations. By calculating $\langle p_A^2 \rangle = (V - s) N_0$, $\langle p_B^2 \rangle = G_p (V + \chi_p) N_0$, $\langle p_A p_B \rangle = G_p^{1/2} \langle p_A^2 \rangle$, we obtain the conditional variance $V(p_B|p_A) = \langle p_B^2 \rangle - |\langle p_A p_B \rangle|^2 / \langle p_A^2 \rangle = G_p (s + \chi_p) N_0$. This equation and the constraint $s \geq V^{-1}$ gives $V(p_B|p_A) \geq G_p (V^{-1} + \chi_p) N_0$, and similarly $V(x_B|x_A) \geq G_x (V^{-1} + \chi_x) N_0$. The bound on $V_{B|A}$ is thus obtained by assuming that Alice may use squeezed or entangled beams, while the bound on $V_{B|E}$ can only be achieved if Eve uses an entangling attack. This reflects the fact that squeezing or entanglement play a crucial role in our security demonstration, even though the protocol implies coherent states. Our security proof addresses individual gaussian attacks only, but as the entangling cloner attack saturates the Heisenberg uncertainty relations, we conjecture that it encompasses all incoherent (non-collective) eavesdropping strategies.

Experimental set-up

A continuous-wave laser diode at 780 nm wavelength associated with an acousto-optic modulator is used to emit 120-ns (full-width at half-maximum) pulses at a 800 kHz rate. The signal pulses contain up to 250 photons, while the local oscillator (LO) power is 1.3×10^8 photons per pulse. The amplitude of each pulse is arbitrarily modulated by an integrated electro-optic modulator. However, owing to the unavailability of a fast phase modulator at 780 nm, the phase is not randomly modulated but scanned continuously. No genuine secret key can be distributed, strictly speaking, but random permutations of Bob's data are used to provide realistic data (see Supplementary Information). The data are organized in bursts of 60,000 pulses, separated by synchronization periods also used to lock the phase of the LO. The overall homodyne detection efficiency is 0.81, due to the optical transmission (0.92), the mode-matching efficiency (0.96) and the photodiode quantum efficiency (0.92). For the critical data at 3 dB loss, the mode-matching efficiency was improved to 0.99, and thus the overall efficiency was 0.84. We also point out that many blocks of data were exchanged around the 3 dB loss point, with a typical rate above 55 kbit s^{-1}.

Secret key distillation

A common bit string is extracted from the continuous data by sequentially reconciling several strings ('slices') of binary functions of the gaussian key elements, applying a binary reconciliation protocol successively on each bit[8,10]. Here, we used five slices, each being corrected either by a trivial one-way protocol (communicating the bits) when the bit error rate (BER) is high, or by the two-way protocol Cascade[27,28] when the BER is low. Note that the disclosed slices are useful for reconciling the remaining slices with less information leaking to Eve, even though they of course do not yield secret bits as such. In addition, Alice and Bob encrypt their classical messages using the one-time pad scheme with a fraction of the previous key bits, or a bootstrap key for the first block. For slices corrected with Cascade, the exchanged parities are encrypted with the same key bits on both sides[29], making Eve aware of the differences between Alice's and Bob's parities (that is, the error positions) but not of their individual values. Fully communicated slices are also encrypted, thereby revealing no information at all to Eve. Still, Eve may exploit the interactivity of Cascade and gain some information on the final key by combining her knowledge of the error positions with that of the correlations between Alice's and Bob's gaussian values. In the present protocol, this information is numerically calculated for an entangling cloner attack, and then destroyed by privacy amplification. This is achieved by appropriate 'hashing'[30] functions (see Supplementary Information). The resulting net secret key rate is then obtained by subtracting, from the raw key rate, the cost of the one-time pad encryption and the error-position information. Finally, we emphasize that sliced reconciliation can be made very close to a one-way protocol by increasing the number of key elements from which the bits are jointly extracted (multidimensional reconciliation[8]). This approach was not implemented here, but should deliver an improved secret key rate, approaching the value from the Csiszár–Körner formula[21,22].

Received 8 July; accepted 30 October 2002; doi:10.1038/nature01289.

1. Braunstein, S. L. & Pati, A. K. *Quantum Information Theory with Continuous Variables* (Kluwer Academic, Dordrecht, in the press).
2. Hillery, M. Quantum cryptography with squeezed states. *Phys. Rev. A* **61,** 022309 (2000).
3. Ralph, T. C. Continuous variable quantum cryptography. *Phys. Rev. A* **61,** 010303(R) (2000).
4. Ralph, T. C. Security of continuous-variable quantum cryptography. *Phys. Rev. A* **62,** 062306 (2000).
5. Reid, M. D. Quantum cryptography with a predetermined key, using continuous-variable Einstein-Podolsky-Rosen correlations. *Phys. Rev. A* **62,** 062308 (2000).
6. Gottesman, D. & Preskill, J. Secure quantum key distribution using squeezed states. *Phys. Rev. A* **63,** 022309 (2001).
7. Cerf, N. J., Lévy, M. & Van Assche, G. Quantum distribution of Gaussian keys using squeezed states. *Phys. Rev. A* **63,** 052311 (2001).
8. Van Assche, G., Cardinal, J. & Cerf, N. J. Reconciliation of a quantum-distributed Gaussian key. Preprint cs.CR/0107030 at ⟨http://arxiv.org⟩ (2001).
9. Bencheikh, K., Symul, Th., Jankovic, A. & Levenson, J. A. Quantum key distribution with continuous variables. *J. Mod. Opt.* **48,** 1903–1920 (2001).
10. Cerf, N. J., Iblisdir, S. & Van Assche, G. Cloning and cryptography with quantum continuous variables. *Eur. Phys. J. D* **18,** 211–218 (2002).
11. Silberhorn, Ch., Korolkova, N. & Leuchs, G. Quantum key distribution with bright entangled beams. *Phys. Rev. Lett.* **88,** 167902 (2002).
12. Silberhorn, Ch., Ralph, T. C., Lütkenhaus, N. & Leuchs, G. Continuous variable quantum cryptography beating the 3 dB loss limit. *Phys. Rev. Lett.* **89,** 167901 (2002).
13. Grosshans, F. & Grangier, Ph. Continuous variable quantum cryptography using coherent states. *Phys. Rev. Lett.* **88,** 057902 (2002).
14. Grosshans, F. & Grangier, Ph. Reverse reconciliation protocols for quantum cryptography with continuous variables. Preprint quant-ph/0204127 at ⟨http://arxiv.org⟩ (2002).
15. Gisin, N., Ribordy, G., Tittel, W. & Zbinden, H. Quantum cryptography. *Rev. Mod. Phys.* **74,** 145–195 (2002).
16. Cerf, N. J., Ipe, A. & Rottenberg, X. Cloning of continuous variables. *Phys. Rev. Lett.* **85,** 1754–1757 (2000).
17. Cerf, N. J. & Iblisdir, S. Optimal N-to-M cloning of conjugate quantum variables. *Phys. Rev. A* **62,** 040301(R) (2000).
18. Grosshans, F. & Grangier, Ph. Quantum cloning and teleportation criteria for continuous quantum variables. *Phys. Rev. A* **64,** 010301(R) (2001).
19. Bennett, C.-H. Quantum cryptography using any two nonorthogonal states. *Phys. Rev. Lett.* **68,** 3121–3124 (1992).
20. Duan, L.-M., Giedke, G., Cirac, J. I. & Zoller, P. Entanglement purification of gaussian continuous variable quantum states. *Phys. Rev. Lett.* **84,** 4002–4005 (2000).
21. Csiszár, I. & Körner, J. Broadcast channel with confidential messages. *IEEE Trans. Inform. Theory* **24,** 339–348 (1978).
22. Maurer, U. M. Secret key agreement by public discussion from common information. *IEEE Trans. Inform. Theory* **39,** 733–742 (1993).
23. Poizat, J.-Ph., Roch, J.-F. & Grangier, Ph. Characterization of quantum non-demolition measurements in optics. *Ann. Phys. (Paris)* **19,** 265–297 (1994).
24. Grangier, Ph., Levenson, J. A. & Poizat, J.-Ph. Quantum non-demolition measurements in optics. *Nature* **396,** 537–542 (1998).
25. Shannon, C. E. A mathematical theory of communication. *Bell Syst. Tech. J.* **27,** 623–656 (1948).
26. Buttler, W. T., Lamoreaux, S. K., Torgerson, J. R., Nickel, G. H. & Peterson, C. G. Fast, efficient error reconciliation for quantum cryptography. Preprint quant-ph/0203096 at ⟨http://arxiv.org⟩ (2002).
27. Brassard, G. & Salvail, L. *Advances in Cryptology — Eurocrypt '93* Lecture Notes in Computer Science (ed. Helleseth, T.) 411–423 (Springer, New York, 1993).
28. Nguyen, K. *Extension des Protocoles de Réconciliation en Cryptographie Quantique* Thesis, Univ. Libre de Bruxelles (2002).
29. Lo, H.-K. Method for decoupling error correction from privacy amplification. Preprint quant-ph/0201030 at ⟨http://arxiv.org⟩ (2002)
30. Bennett, C. H., Brassard, G., Crépeau, C. & Maurer, U. M. Generalized privacy amplification. *IEEE Trans. Inform. Theory* **41,** 1915–1935 (1995).

Supplementary Information accompanies the paper on *Nature*'s website (➧ **http://www.nature.com/nature**).

Acknowledgements The contributions of J. Gao to the early stages of the experiment, and of K. Nguyen to the software development, are acknowledged. We thank S. Iblisdir for discussions, and Th. Debuisschert for the loan of the 780 nm integrated modulator. This work was supported by the EU programme IST/FET/QIPC (projects "QUICOV" and "EQUIP"), the French programmes ACI Photonique and ASTRE, and by the Belgian programme ARC.

Competing interests statement The authors declare that they have no competing financial interests.

Correspondence and requests for materials should be addressed to P.G. (e-mail: philippe.grangier@iota.u-psud.fr).

Single-nanowire electrically driven lasers

Xiangfeng Duan*†, Yu Huang*†, Ritesh Agarwal* & Charles M. Lieber*‡

** Department of Chemistry and Chemical Biology, ‡ Division of Engineering and Applied Sciences, Harvard University, Cambridge, Massachusetts 02138, USA*
† These authors contributed equally to this work

Electrically driven semiconductor lasers are used in technologies ranging from telecommunications and information storage to medical diagnostics and therapeutics[1]. The success of this class of lasers is due in part to well-developed planar semiconductor growth and processing, which enables reproducible fabrication of integrated, electrically driven devices[2,3]. Yet this approach to device fabrication is also costly and difficult to integrate directly with other technologies such as silicon microelectronics. To overcome these issues for future applications, there has been considerable interest in using organic molecules[4,5], polymers[6,7],

and inorganic nanostructures[8–10] for lasers, because these materials can be fashioned into devices by chemical processing. Indeed, amplified stimulated emission and lasing have been reported for optically pumped organic systems[4–7] and, more recently, inorganic nanocrystals[8,9] and nanowires[10]. However, electrically driven lasing, which is required in most applications, has met with several difficulties in organic systems[11], and has not been addressed for assembled nanocrystals or nanowires. Here we investigate the feasibility of achieving electrically driven lasing from individual nanowires. Optical and electrical measurements made on single-crystal cadmium sulphide nanowires show that these structures can function as Fabry–Perot optical cavities with mode spacing inversely related to the nanowire length. Investigations of optical and electrical pumping further indicate a threshold for lasing as characterized by optical modes with instrument-limited linewidths. Electrically driven nanowire lasers, which might be assembled in arrays capable of emitting a wide range of colours, could improve existing applications and suggest new opportunities.

Free-standing semiconductor nanowires, which can be prepared as single crystals with controlled diameters by metal nanocluster catalysed growth[12–14], are attractive building blocks for creating electrically driven lasers because their defect-free structures exhibit the superior electrical transport of high-quality planar inorganic devices[15–17], and because a single nanowire can function as a stand-alone optical cavity and gain medium. Here we focus on single-crystal, 80–200 nm diameter cadmium sulphide (CdS) nanowires that have a wurtzite structure with a [001] growth axis. In general, a nanowire will function as a single-mode optical waveguide[18] (Fig. 1a) when $1 \approx (\pi D/\lambda)(n_1^2 - n_0^2)^{0.5} < 2.4$, where 1 is a practical lower limit, D is the nanowire diameter, λ is the wavelength, and n_1 and n_0 are the refractive indices of the nanowire and surrounding medium, respectively. In the case of CdS nanowires ($n_1 \approx 2.5$, $\lambda \approx 510$ nm, 300 K), the minimum diameter needed to support a single mode is of the order of 70 nm. If the ends of the nanowire are cleaved, they can function as two reflecting mirrors that define a Fabry–Perot optical cavity with modes $m(\lambda/2n_1) = L$, where m is an integer and L is the length of the cavity. Significantly, transmission and scanning electron microscopy studies show that solution-phase sonication of CdS nanowires produces a high (>50%) yield of flat ends (Fig. 1b), indicative of cleavage perpendicular to the [001] growth direction. These results suggest that a substantial number of nanowires should function as Fabry–Perot cavities.

The optical cavity properties of the CdS nanowires, which are central to our use of these nanostructures for lasers, were characterized by photoluminescence measurements at the single nanowire level using a far-field epifluorescence microscope[19]. A typical room-temperature luminescence image (Fig. 1c) of a CdS nanowire excited with a tightly focused laser about 15 μm from the nanowire end shows strong emission at the excitation focus and also prominent emission near the nanowire end. Studies of several nanowires show that outside the excitation region emission is only observed from the nanowire ends, thus suggesting that these CdS nanowires function as waveguides.

To further probe the nanowire cavity properties, spectroscopy measurements have been made at different regions as a function of excitation power under uniform illumination. At low power, photoluminescence spectra recorded from the body exhibit a broad peak with a maximum at 512 nm and a full-width at half-maximum (FWHM) of 24 nm (Fig. 1d). The peak maximum is consistent with room-temperature band-edge emission from CdS, and contrasts with the deep-level emission at around 600 nm that usually dominates epitaxial CdS thin films[20]. Spectra recorded from the nanowire end at low excitation power showed a relatively broad peak that was red-shifted about 30 nm relative to spectra from the body. The observed spectra red-shift is consistent with re-absorption of band-edge emission within the CdS nanowire cavity.

Photoluminescence measurements made at higher excitation powers reveal other important features about the CdS nanowire cavities (Fig. 1e). First, the nanowire end emission blue-shifts towards the band edge as the re-absorption is partially saturated with increasing excitation power. Second, the end-emission intensity increases superlinearly with excitation power, whereas emission from the nanowire body exhibits a slight, approximately linear increase. Third, periodic variations in the intensity, which are suggestive of the longitudinal modes of a Fabry–Perot cavity, are observed. For a cavity of length L, the mode spacing, $\Delta\lambda$, is given by

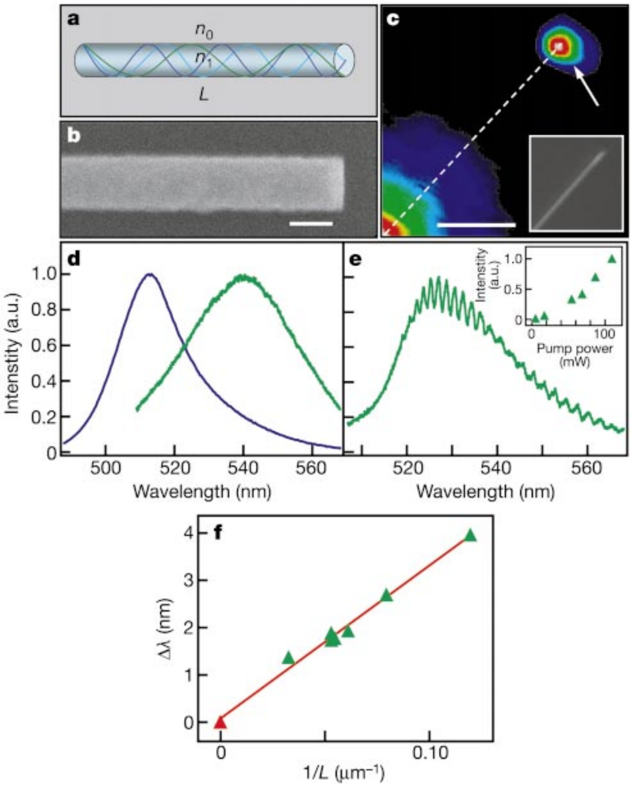

Figure 1 Nanowire Fabry–Perot optical cavities. **a**, Schematic showing a nanowire as an optical waveguide, and with cleaved ends defining a Fabry–Perot cavity. **b**, SEM image of a cleaved CdS nanowire end. Scale bar, 100 nm. **c**, Room-temperature photoluminescence image of a CdS nanowire excited (low-left corner, power 10 mW) about 15 μm away from the nanowire end. The white arrow and dashed line highlight the nanowire end and axis, respectively. Scale bar, 5 μm. Inset, an optical image of the nanowire obtained with white-light illumination. **d**, Photoluminescence spectra obtained from the body of the nanowire (blue) and the end of the nanowire (green) at low pump power (10 mW). **e**, Spectrum from the nanowire end at higher pump power (80 mW) exhibiting periodic intensity variation. The period varies from 1.67 to 2.59 nm with increasing wavelength, which is consistent with the calculated mode spacing for the 18.8 μm nanowire and the dispersion of the refractive index, $n(\lambda)$ (ref. 25). Inset, end-emission intensity as a function of pump power. The nanowires in **d** and **e** were uniformly illuminated. **f**, Mode spacing versus inverse nanowire length. Green triangles, experimental points; red triangle, extrapolation to infinite length; red line, linear fit to these data. The contribution of $n(\lambda)$ was minimized by plotting the mode spacing at 530 nm in all cases. CdS nanowires were synthesized at 880 °C by laser-assisted catalytic growth[12–14] using gold as the catalyst. The resulting nanowire product was dispersed in ethanol, and sonicated for 30–60 s to produce a high yield of wires with cleaved ends. Room- and low-temperature luminescence measurements were made with homebuilt epifluorescence microscopes, where a frequency-doubled Ti:sapphire laser (76 MHz, ~200 fs pulses, 410 nm) was used for optical excitation. Spectra were recorded using a 300 mm spectrometer (1200 lines mm^{-1} grating) and liquid-nitrogen-cooled charge-coupled device (CCD) detector. The room- and low-temperature instruments have spectral resolutions of 0.3 and 0.8 nm, respectively.

$(\lambda^2/2L)(n_1 - \lambda(\mathrm{d}n_1/\mathrm{d}\lambda))^{-1}$, where $\mathrm{d}n_1/\mathrm{d}\lambda$ is the dispersion relation for the refractive index. This expression provides a good description of the observed spacing when the measured nanowire length is equated with L, and moreover, analysis of similar data from nanowires of varying length demonstrates that the mode spacing is inversely proportional to the wire length (Fig. 1f), as expected. Together these results show that the CdS nanowires form a Fabry–Perot cavity. From the mode linewidths (background subtracted) we estimate a moderate cavity quality factor of about 600 at room temperature.

The observation of sharp modes in the uniform CdS nanowire gain medium in the superlinear regime is indicative of amplified spontaneous emission. Significantly, excitation at higher powers, which was possible in low-temperature experiments, leads to preferential gain in a single mode and the onset of lasing (Fig. 2a). Measurements of the linewidth dependence on pump power show an abrupt decrease to a value limited by our instrument resolution soon after the changeover to superlinear behaviour (Fig. 2b). In contrast, emission from the nanowire body is broad and approximately linearly dependent on excitation power, and the background spontaneous emission saturates in the superlinear regime (Supplementary Information). From the superlinear behaviour we estimate the threshold average pump power to be 40 kW cm^{-2}, although the threshold varies from nanowire to nanowire with the lowest value to date of around 2 kW cm^{-2} at low temperature.

These optical experiments demonstrate that individual nanowires can function as Fabry–Perot cavities and support lasing, although without electrical pumping nanowire lasers would be of limited technological importance[1–3]. In general, electrically driven lasing requires efficient electron (n-type) and hole (p-type) injection into the cavity region. In the case of planar CdS structures, this has been difficult owing to problems in producing high-mobility p-type CdS or combining n-CdS with other high-mobility p-type materials. A clear advantage of nanowire-based structures is the ability to combine different high-quality materials as desired to achieve the required device function[15–17].

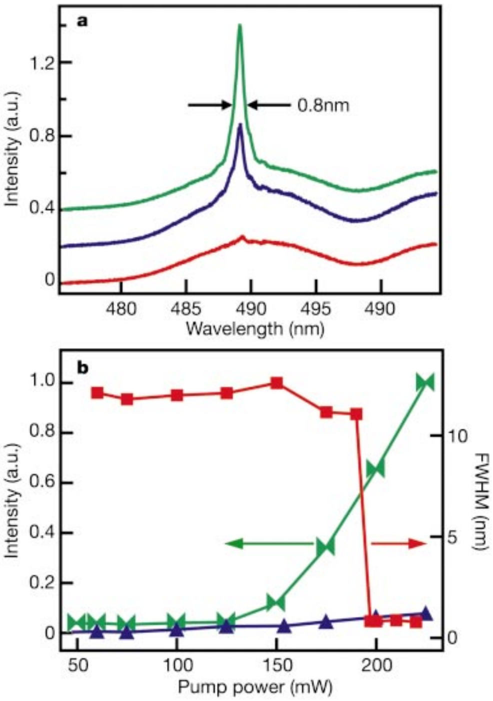

Figure 2 Optically pumped nanowire laser. **a**, Emission spectra from a CdS nanowire end with a pump power of 190, 197 and 200 mW (red, blue and green) recorded at 8 K. The spectra are offset by 0.2 intensity units for clarity. **b**, Emission intensity and FWHM of emission peaks versus laser pump power. The emission intensity from the nanowire body (blue) maintains a low value and is approximately linear in pump power, whereas the emission from the nanowire end (green) exhibits superlinear behaviour above 125 mW. The FWHM (red) has a nearly constant value of about 12 nm at low power, and abruptly narrows to the instrument-resolution value at high power. Solid symbols correspond to experimental data and lines are guides to the eye.

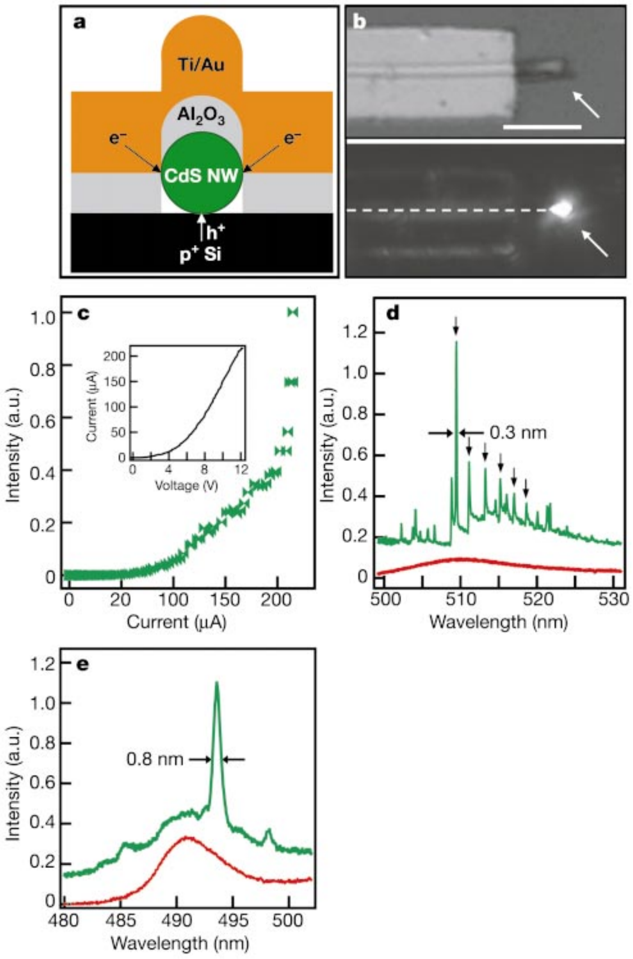

Figure 3 Nanowire electrical injection laser. **a**, Schematic showing the cross-section of the device structure. In this structure, electrons and holes can be injected into the CdS nanowire along the whole length from the top metal layer and the bottom p-Si layer, respectively. The devices were fabricated by assembling CdS nanowires on heavily doped p-Si on insulator substrates ($>4 \times 10^{19}$ cm^{-3}; 500 nm thick), followed by electron-beam lithography and electron-beam evaporation of 60–80 nm aluminium oxide, 40 nm Ti and 200 nm Au. One end of the nanowire was left uncovered for emission output from the device. **b**, Top panel shows an optical image of a device described in **a**. The arrow highlights the exposed CdS nanowire end. Scale bar, 5 μm. Bottom panel shows an electroluminescence image recorded from this device at room temperature with an injection current of about 80 μA. The arrow highlights emission from the CdS nanowire end. The dashed line highlights the nanowire position. **c**, Emission intensity versus injection current. The intensity increases rapidly above about 200 μA, which corresponds to the onset of lasing. Inset shows current versus voltage for this device. **d**, Electroluminescence spectra obtained from the nanowire end with injection currents of 120 μA (red) and 210 μA (green). The black arrows highlight Fabry–Perot cavity modes with an average spacing of 1.83 nm. The green spectrum is shifted upwards by 0.15 intensity units for clarity. **e**, Emission spectra from a CdS nanowire device with injection currents of 200 μA (red) and 280 μA (green) recorded at 8 K. The spectra are offset by 0.10 intensity units for clarity. The single peak observed at high injection has a linewidth of 0.8 nm, comparable to the instrument resolution and that observed in the optical pumping experiments.

Initial studies of electrical injection into CdS nanowire cavities were carried out using n-type CdS and p-type silicon (p-Si) crossed-nanowire structures[15–17]. Transport studies of individual CdS nanowires show that they are n-type with doping concentrations on the order of 10^{18}–$10^{19}\,\mathrm{cm}^{-3}$ and electron mobilities of about $100\,\mathrm{cm}^2\,\mathrm{V}^{-1}\,\mathrm{s}^{-1}$ (Supplementary Information). Current–voltage (*I*–*V*) measurements made on a typical n-CdS/p-Si crossed nanowire structure show current rectification with a sharp forward-bias turn-on at about 2 V, consistent with the formation of a p–n diode (see Supplementary Information for band diagram of this heterostructure). In forward bias, these crossed-nanowire structures exhibit electroluminescence from the n-CdS/p-Si nanowire crosspoint and stronger emission from the ends of the CdS nanowires, which is consistent with the CdS nanowires functioning as good waveguides. Electroluminescence spectra recorded from CdS nanowire ends exhibit a prominent modulation in the intensity that can be assigned to the longitudinal modes of nanowire Fabry–Perot cavities (our unpublished results), and thus these electroluminescence data are in agreement with our optically pumped data recorded (Fig. 1) from similar CdS nanowires.

To investigate nanowire injection lasers we have implemented a hybrid structure (Fig. 3a) in which the n-type CdS nanowire laser cavities are assembled onto p-Si electrodes defined in heavily p-doped planar substrates. This structure produces the n-CdS/p-Si heterojunction (Supplementary Information) needed for an injection device. The hybrid structure is analogous to the p–n diodes formed in the crossed n-CdS/p-Si nanowire devices, although in this case holes can be injected along the entire length of the CdS nanowire cavity in contrast to the single crosspoint in crossed-nanowire devices. An image of a typical device is shown in Fig. 3b. Current versus voltage data recorded from devices fabricated in this way show current rectification with a forward-bias turn-on of 2–5 V (inset, Fig. 3c and Supplementary Information), which is consistent with the formation of p–n diodes. The variation in turn-on voltage is believed to be due to Al_2O_3 barrier between the metal/CdS contact and/or oxide at the CdS/p-Si junction.

Images of the room-temperature electroluminescence produced in forward bias from these hybrid structures (Fig. 3b) exhibit strong emission from the exposed CdS nanowire ends. Measurements of the nanowire end electroluminescence intensity versus current (Fig. 3c) show an initial increase in the intensity at about 90 μA and then a much more rapid and highly nonlinear increase at about 200 μA. Significantly, at low injection currents the spectrum of the end emission (Fig. 3d) shows a broad peak with FWHM $\approx$ 18 nm, consistent with spontaneous emission, but above the 200 μA threshold the spectrum quickly collapsed into a limited number of very sharp peaks with a dominant emission line at 509.6 nm (Fig. 3d). These sharp peaks emerge from only part of the spontaneous emission spectrum and had an average spacing of about 1.8 nm, which is consistent with the Fabry–Perot cavity modes for the length of the nanowire device. The observation of multiple peaks versus a single mode is often observed in studies of lasing in planar devices[20] pumped close to threshold. Other small, sharp peaks are also observed and their explanation will require more detailed consideration of the nanowire cavity. Lastly, the dominant mode has a linewidth limited by the instrument resolution of only 0.3 nm. Taken together, these observations provide strong evidence for lasing from single-nanowire injection structures at room temperature.

There are several additional points and experiments we have carried out that deserve comment. First, we believe that injection non-uniformity, which is due in part to non-ideal CdS/p-Si and metal/CdS junctions, limits these new lasers. For example, at present it is not possible to drive the devices substantially above the observed threshold for lasing, which would allow for better characterization of threshold behaviour and also would be expected to lead to single-mode output. Second, we have also carried out low-temperature measurements on independent CdS injection laser devices. These data (Fig. 3e) clearly show that the spontaneous emission spectrum can collapse to a single instrument-resolution-limited mode that is characteristic of lasing; moreover, these results are very similar to the low-temperature optically pumped results (Fig. 2). Our studies suggest that with further improvements in nanowire laser assembly/fabrication, better optical quality and greater robustness will be possible. Third, the measurement geometry, in which emitted light is collected perpendicularly to the nanowire cavity axis, contributes to background signal above the lasing threshold[21] and complicates determination of absolute current–intensity relationship for the nanowire lasers. We believe that future studies of these structures with emission collected in an end-on geometry could provide data of use for developing a quantitative understanding and improved performance of these injection lasers.

Our results show that nanoscale injection lasers can be made from single semiconductor nanowires, and describe a powerful approach for producing integrated electrically driven photonic devices. This basic approach, which relies upon bottom-up assembly of the key laser cavity/medium in a single step, can be extended to other materials, such as GaN[22] and InP[15] nanowires, to produce nanoscale lasers that not only cover the ultraviolet through near-infrared spectral regions but can also be integrated as single or multi-colour laser source arrays in silicon microelectronics and lab-on-a-chip devices. There are some scientific and technical challenges that may need to be addressed to realize this potential, such as the development of more efficient cavities and injection schemes. We believe that both issues could be addressed at the nanowire growth stage before device assembly by preparing Bragg gratings at the nanowire ends through axial composition modulation[23], and using core–shell nanowire structures[24] to enable uniform injection into the active medium/cavity, respectively. By addressing these and other issues, such as quantifying contributions to optical losses within the nanowire cavity, nanowire lasers could be developed into systems that affect several applications for solid-state lasers, including telecommunications and data storage, and may enable new applications in highly integrated chemical/biological sensors, near-field optical lithography, a host of scanning probe microscopies, and perhaps even laser-based surgery with unprecedented resolution. ☐

Received 1 November; accepted 29 November 2002; doi:10.1038/nature01353.

1. Gray, G. R. in *Semiconductor Laser: Past, Present, and Future* (ed. Agrawal, G. P.) 284–320 (American Institute of Physics, New York, 1995).
2. Kapon, E. (ed.) *Semiconductor Lasers I: Fundamentals* (Academic, San Diego, 1999).
3. Kapon, E. (ed.) *Semiconductor Lasers II: Materials and Structures* (Academic, San Diego, 1999).
4. Kozlov, V. G., Bulovic, V., Burrows, P. E. & Forrest, S. R. Laser action in organic semiconductor waveguide and double-heterostructure devices. *Nature* **389,** 362–363 (1997).
5. Bergren, M., Dodabalapur, A., Slusher, R. E. & Bao, Z. Light amplification on organic thin films using cascade energy transfer. *Nature* **389,** 466–469 (1997).
6. Tessler, N., Denton, G. J. & Friend, R. H. Lasing from conjugated-polymer microcavities. *Nature* **382,** 695–697 (1996).
7. Hide, F. *et al.* Semiconductor polymers: A new class of solid state laser materials. *Science* **273,** 1833–1836 (1996).
8. Klimov, V. I. *et al.* Optical gain and stimulated emission in nanocrystal quantum dots. *Science* **290,** 314–317 (2000).
9. Kazes, M., Lewis, D. Y., Ebenstein, Y., Mokari, T. & Banin, U. Lasing from semiconductor quantum rods in a cylindrical microcavity. *Adv. Mater.* **14,** 317–321 (2002).
10. Huang, H. M. *et al.* Room-temperature ultraviolet nanowire nanolasers. *Science* **292,** 1897–1899 (2001).
11. Kozlov, V. G. *et al.* Structures for organic laser diode lasers and optical properties of organic semiconductor under intense optical and electrical excitations. *IEEE J. Quant. Elec.* **36,** 18–26 (2000).
12. Morales, A. M. & Lieber, C. M. A laser ablation method for the synthesis of crystalline semiconductor nanowires. *Science* **279,** 208–211 (1998).
13. Duan, X. & Lieber, C. M. General synthesis of compound semiconductor nanowires. *Adv. Mater.* **12,** 298–302 (2000).
14. Gudiksen, M. S. & Lieber, C. M. Diameter selective synthesis of semiconductor nanowires. *J. Am. Chem. Soc.* **122,** 8801–8802 (2000).
15. Duan, X., Huang, Y., Wang, J., Cui, Y. & Lieber, C. M. Indium phosphide nanowires as building blocks for nanoscale electronic and optoelectronic devices. *Nature* **409,** 66–69 (2001).
16. Cui, Y. & Lieber, C. M. Functional nanoscale electronic devices assembled using silicon nanowire building blocks. *Science* **291,** 891–893 (2001).

17. Huang, Y. *et al.* Logic gates and computation from assembled nanowire building blocks. *Science* **294,** 1313–1317 (2001).
18. Chen, C.-L. *Elements of Optoelectronics and Fiber Optics* (Irwin, Chicago, 1996).
19. Wang, J., Gudiksen, M. S., Duan, X., Cui, Y. & Lieber, C. M. Highly polarized photoluminescence and polarization sensitive photodetectors from single indium phosphide nanowires. *Science* **293,** 1455–1457 (2001).
20. Bagnall, D. M., Ullrich, B., Sakai, H. & Segawa, Y. Micro-cavity lasing of optically excited CdS thin films at room temperature. *J. Cryst. Growth.* **214/215,** 1015–1018 (2000).
21. Bagnell, D. M., Ullrich, B., Qiu, X. G., Segawa, Y. & Sakai, H. Microcavity lasing of optically excited cadmium sulphide thin films at room temperature. *Opt. Lett.* **24,** 1278–1280 (1999).
22. Huang, Y., Duan, X., Cui, Y. & Lieber, C. M. GaN nanowire nanodevices. *Nano Lett.* **2,** 101–104 (2002).
23. Gudiksen, G. S., Lauhon, L. J., Wang, J., Smith, D. & Lieber, C. M. Growth of nanowire superlattice structures for nanoscale photonics and electronics. *Nature* **415,** 617–620 (2002).
24. Lauhon, L. J., Gudiksen, M. S., Wang, D. & Lieber, C. M. Epitaxial core-shell and core-multishell nanowire heterostructures. *Nature* **420,** 57–61 (2002).
25. El Assali, K. *et al.* Some structural and optical properties of CdS thin films prepared by RF sputtering. *Phys. Status Solidi A* **178,** 701–708 (2000).

Supplementary Information accompanies the paper on *Nature*'s website (**http://www.nature.com/nature**).

Acknowledgements We thank H. Park, X. Zhuang & M. S. Gudiksen for helpful discussion. C.M.L. is grateful for support of this work by the Air Force Office of Scientific Research.

Competing interests statement The authors declare that they have no competing financial interests.

Correspondence and requests for materials should be addressed to C.M.L. (e-mail: cml@cmliris.harvard.edu).

Rapid Cenozoic glaciation of Antarctica induced by declining atmospheric CO_2

Robert M. DeConto* & David Pollard†

* *Department of Geosciences, University of Massachusetts, Amherst, Massachusetts 01003, USA*
† *EMS Environment Institute, The Pennsylvania State University, University Park, Pennsylvania 16802, USA*

The sudden, widespread glaciation of Antarctica and the associated shift towards colder temperatures at the Eocene/Oligocene boundary ($\sim$34 million years ago) (refs 1–4) is one of the most fundamental reorganizations of global climate known in the geologic record. The glaciation of Antarctica has hitherto been thought to result from the tectonic opening of Southern Ocean gateways, which enabled the formation of the Antarctic Circumpolar Current and the subsequent thermal isolation of the Antarctic continent[5]. Here we simulate the glacial inception and early growth of the East Antarctic Ice Sheet using a general circulation model with coupled components for atmosphere, ocean, ice sheet and sediment, and which incorporates palaeogeography, greenhouse gas, changing orbital parameters, and varying ocean heat transport. In our model, declining Cenozoic CO_2 first leads to the formation of small, highly dynamic ice caps on high Antarctic plateaux. At a later time, a CO_2 threshold is crossed, initiating ice-sheet height/mass-balance feedbacks that cause the ice caps to expand rapidly with large orbital variations, eventually coalescing into a continental-scale East Antarctic Ice Sheet. According to our simulation the opening of Southern Ocean gateways plays a secondary role in this transition, relative to CO_2 concentration.

Antarctica has been located over southern polar latitudes since the Early Cretaceous[6], yet is thought to have remained mostly ice-free, vegetated, and with mean annual temperatures well above freezing until the Eocene/Oligocene boundary[4,7]. Evidence for cooling and the sudden growth of an East Antarctic Ice Sheet (EAIS) comes from marine records (refs 1–3), in which the gradual cooling from the presumably ice-free warmth of the Early Tertiary to the cold 'icehouse' of the Late Cenozoic is punctuated by a sudden >1.0‰ rise in benthic δ^{18}O values at $\sim$34 million years (Myr). More direct evidence of cooling and glaciation near the Eocene/Oligocene boundary is provided by drilling on the East Antarctic margin[8], the record of circum-Antarctic ice-rafted debris[9], a shift in the clay composition of circum-Antarctic sediments[10], and the fossil record of Antarctic vegetation[11]. Glaciation is believed to have begun in the East Antarctic interior, discharging mainly via the Lambert Graben to Prydz Bay, with the Transantarctic Mountains restricting ice flow towards the Ross Sea until the ice sheets became larger in the Middle Oligocene[4]. Palaeogene Antarctic ice sheets appear to have been temperate, highly dynamic[7,12], and paced by Milankovitch orbital parameters[1,13] in much the same way as the Quaternary ice sheets of the Northern Hemisphere.

The initial growth of the EAIS near the Eocene/Oligocene boundary has been attributed to the tectonic opening of ocean gateways between Antarctica and Australia (Tasmanian Passage), and Antarctica and South America (Drake Passage), leading to the organization of the Antarctic Circumpolar Current (ACC) and the 'thermal isolation' of Antarctica[5,14]. This notion is supported by ocean general circulation model (OGCM) simulations, showing that the opening of Drake Passage and the organization of an ACC reduces southward oceanic heat transport and cools Southern Ocean sea surface temperatures (SSTs) by $\sim$3 °C (refs 15, 16). However, although most tectonic reconstructions place the opening of the Tasmanian Passage close to the Eocene/Oligocene boundary, Drake Passage may not have provided a significant deep-water passage until several million years later[17,18]. Additionally, these OGCM simulations lacked realistic atmospheric components, so the effects on Antarctic climate are unresolved.

Alternatively, declining atmospheric CO_2 may have played a

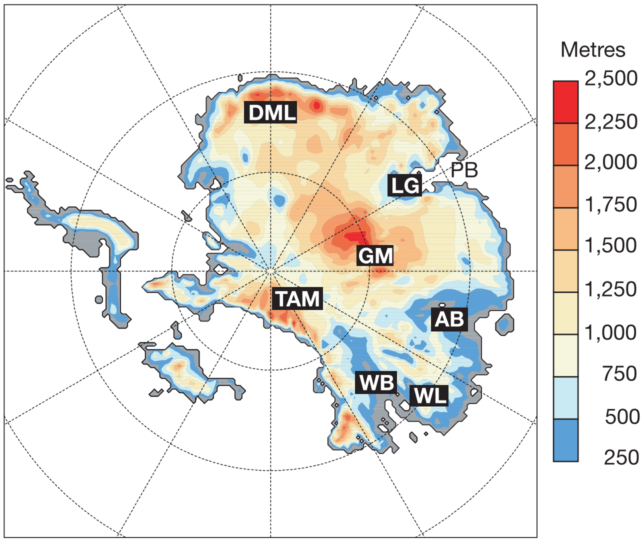

Figure 1 Early Cenozoic ice-free Antarctic topography in metres above sea level. This was reconstructed from a modern 5-km database[30], isostatically relaxed to ice-free equilibrium and interpolated to the 40-km polar stereographic grid of the ice-sheet model. Abbreviated place names mentioned in the text are also shown: AB, Aurora Basin; DML, Dronning Maud Land; GM, Gamburtsev Mountains; LG, Lambert Graben; PB, Prydz Bay; TAM, Transantarctic Mountains; WB, Wilkes Basin; WL, Wilkes Land.

Copyright © 2003 EBSCO Publishing